Article

Optical Constants of Crystallized TiO₂ Coatings Prepared by Sol-Gel Process

Xiaodong Wang *, Guangming Wu, Bin Zhou and Jun Shen *

Shanghai Key Laboratory of Special Artificial Microstructure Materials and Technology,
Pohl Institute of Solid State Physics, Tongji University, Siping Road 1239, Shanghai 200092, China;
E-Mails: wugm@tongji.edu.cn (G.W.); zhoubin863@tongji.edu.cn (B.Z.)

* Authors to whom correspondence should be addressed;
E-Mails: xiaodong_wang@tongji.edu.cn (X.W.); shenjun67@tongji.edu.cn (J.S.);
Tel.: +86-(0)21-6598-2762 (X.W.); Fax: +86-(0)21-6598-6071 (X.W.).

Abstract: Titanium oxide coatings have been deposited by the sol-gel dip-coating method. Crystallization of titanium oxide coatings was then achieved through thermal annealing at temperatures above 400 ℃. The structural properties and surface morphology of the crystallized coatings were studied by micro-Raman spectroscopy and atomic force microscopy, respectively. Characterization technique, based on least-square fitting to the measured reflectance and transmittance spectra, is used to determine the refractive indices of the crystallized TiO₂ coatings. The stability of the synthesized sol was also investigated by dynamic light scattering particle size analyzer. The influence of the thermal annealing on the optical properties was then discussed. The increase in refractive index with high temperature thermal annealing process was observed, obtaining refractive index values from 1.98 to 2.57 at He-Ne laser wavelength of 633 nm. The Raman spectroscopy and atomic force microscopy studies indicate that the index variation is due to the changes in crystalline phase, density, and morphology during thermal annealing.

1. Introduction

Titanium oxide (TiO$_2$) coatings have been extensively studied and used owing to their great potential in optical device application, such as planar waveguides [1], antireflective coatings [2,3], and solar cells [4–6]. Various methods are available for the preparation of the TiO$_2$ coatings, such as electron-beam evaporation [7,8], sputtering [9,10], pulsed laser deposition [11–13], chemical spray pyrolysis [14], chemical vapor deposition [15,16], and the sol-gel method [17–21]. Among the different techniques, the sol-gel method seems to be the most promising one as it offers the advantages of macro-porous coatings prepared at a comparatively low cost, capability of large coating size, and relatively easy process control [22].

As sol-gel method is a type of wet chemical method, the as-deposited coating is amorphous. Thermal annealing can be used for crystallization of TiO$_2$ coatings, which will endow the TiO$_2$ coating with higher refractive index [23], self-cleaning property [24], and photo-catalytic activity [25]. For sol-gel derived TiO$_2$ coating, the high porosity combined with the existence of residual organic components make the optical constants of coating layer quite different from that of solid coating and bulk materials. Therefore, it is very important to determine the optical constants for sol-gel derived coatings systemically. In our previous work [26], the optical constants of amorphous TiO$_2$ coatings were determined by spectroscopic ellipsometry, and these amorphous TiO$_2$ coatings have been successfully used for fabrication of two-layer antireflective coatings [3]. However, the reports available for optical constants of crystallized sol-gel TiO$_2$ coatings are scarce and not yet taken seriously. It is of interest to study the optical constants of the crystallized sol-gel TiO$_2$ coatings. Hence, we performed this work to understand the optical properties of crystallized sol-gel TiO$_2$ coatings more systemically and deeply. The TiO$_2$ coatings are prepared by sol-gel dip-coating method and annealed between 400 and 900 °C. The variation of the refractive index of the coatings was measured through spectrometer and optical model fitting. Raman spectroscopy was conducted to explore the crystalline nature of the coating. The atomic force microscope (AFM) was used to measure the surface morphology. The crystalline structure, surface morphology, and optical properties of the TiO$_2$ coatings were then studied and discussed. We demonstrated that the increase in refractive index was due to combined effects of crystalline phase, density, and morphology during thermal annealing.

2. Experimental Section

2.1. TiO$_2$ Sol Synthesis

The flow chart of the TiO$_2$ sol synthesis process is shown in Figure 1. Tetrabutyl titanate (Ti(OC$_4$H$_9$)$_4$, TBOT) was selected as precursor, with anhydrous ethanol (C$_2$H$_5$OH, EtOH) as solvent, deionized water for hydrolysis, acetylacetone (CH$_3$COCH$_2$COCH$_3$, AcAc) as chelating agent and acetic acid (CH$_3$COOH, HAc) as catalyst. During synthesis, two different but equal parts of ethanol solutions were prepared. In the first part, TBOT was dissolved into anhydrous ethanol containing AcAc. After mixing with HAc, the solution was then sealed and kept stirring for 30 min to achieve a complete chelation between the alkoxide and AcAc. The second part of the solution was then prepared by mixing the deionized water with anhydrous ethanol. These two solutions were then mixed and stirred for 2 h to achieve hydrolysis and condensation. The molar ratio was

TBOT:EtOH:H$_2$O:HAc:AcAc = 1:30:3:2:1. The mixture was finally aged in a stable environment (with humidity lower than 30% and temperature of 20~25 ℃) for 72 h.

Figure 1. Flow chart of TiO$_2$ sol synthesis process.
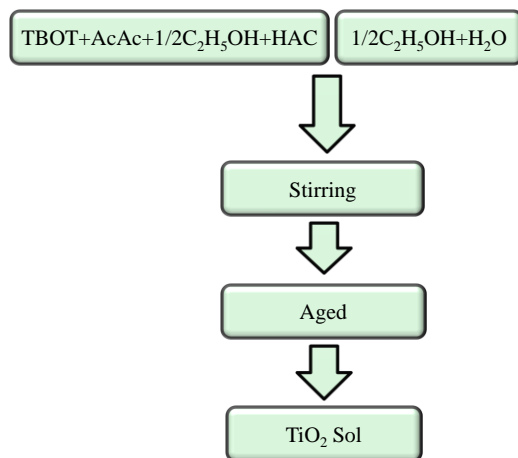
2.2. Coating Preparation

The silicon wafer and silica glass substrates were firstly cleaned thoroughly, heated at 200 ℃ for 20 min, and then cooled down to room temperature. A dip-coating apparatus (CHEMAT Dip Master-200) was used for the depositions, and the coating thickness could be adjusted by the withdrawal rate (0~12 inch/min). After each coating, the coatings were first pretreated at 100 ℃ for 1 h, and then heat-treated in a muffle furnace for 2 h at different temperatures, ranging from 300 to 900 ℃. All the coating processes of the samples were the same to make sure the properties of coatings annealed at different temperatures can be compared and studied.

2.3. Characterization

Particle size distribution of TiO$_2$ sol was analyzed using a dynamic light scattering particle size analyzer (HORIBA LB-550). Raman spectra were recorded at room temperature with a JOBIN-YVON micro-Raman apparatus (HR-800) equipped with a 30 mW He-Cd laser (KIMMON KOHA, IK3301R-G) emitting at 325 nm, and a microscope (OLYMPUS BX41). An edge filter was used in the Raman setup to block the Rayleigh scattering light and stray laser bands. The laser beam irradiating the sample was attenuated to below 0.1 mW in order to avoid laser-induced heating. Before each measurement, a standard silicon wafer was used for the wavenumber calibration of the spectrometer. The spectral resolution was estimated to be 1.6 cm^{-1}. The transmittance and reflectance spectra of the coatings were measured in the 400~1000 nm region using a JASCO-V570 UV-VIS-NIR double beam spectrometer. The surface morphology of the coatings was characterized using AFM (PSIA XE-100).

3. Results and Discussion

3.1. Structural Properties

Figure 2 shows the micro-Raman spectra of the TiO_2 coatings annealed at different temperatures. It can be seen from the figure that crystallization does not start until the annealing temperature reaches 400 ℃. Raman spectra of the coatings annealed at temperatures higher than 400 ℃ exhibit clearly lines characteristic of anatase TiO_2 phase at 141, 194, 394, 515, and 636 cm^{-1}. The intensity of these lines increases with increasing annealing temperature. For temperature up to 800 ℃, besides the peaks characteristic of the anatase phase, the new Raman peaks at 144, 235, 443, 610, and 824 cm^{-1} that come from the rutile TiO_2 are also observed, which means that the coatings were composed of anatase and rutile structures at this temperature. The observed band positions are in complete accordance with those reported in previous studies for anatase and rutile powder and single crystals [22,27,28]. At 900 ℃, the peaks from anatase TiO_2 disappear, indicating the completion of the transformation of TiO_2 coatings from anatase to rutile phase.

Figure 2. Raman spectra of TiO_2 coatings annealed at different temperatures.
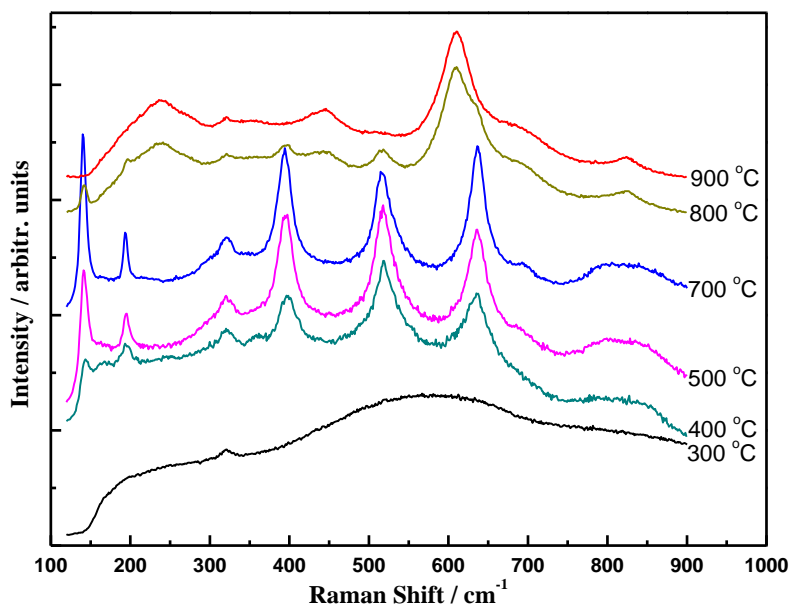
3.2. Optical Properties

Transmittance spectra of the coatings annealed at various temperatures in the wavelength region from 300 to 1000 nm are presented in Figure 3. Silica glasses were used as the substrate in these experiments to avoid the influence of the absorption edge of the substrate. As shown in Figure 3, the average transmittance of 400 ℃ annealed TiO_2 coatings is about 80% in the visible region with respect to silica glass substrate. Annealing shows a slight decrease in transmittance with the increasing annealing temperature. The coatings annealed above 700 ℃ shows a significant decrease in visible light transmittance. It can be attributed to the densification and the crystalline transformation that increase the refractive index of the TiO_2 coatings. Then the refractive index has been determined to see the direct effect of densification and crystalline structure.

Figure 3. Transmittance spectra of TiO$_2$ coatings annealed at different temperatures.
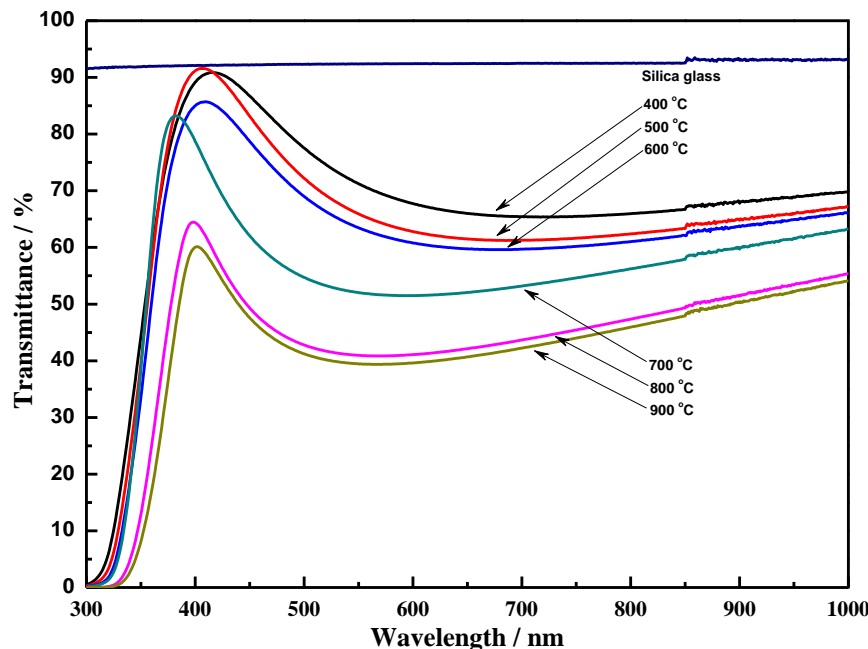
The determination of the refractive index of the coatings can be inferred from the spectroscopic measurements. For sol-gel dip-coating technology, both sides of the glass substrates were coated. Therefore, we built a five layer (Air/TiO$_2$ layer/Silica glass/TiO$_2$ layer/Air) structure model to determine the optical constants of the coating. The Cauchy formula [29], which is an optical model for insulators and dielectric coatings, was used to describe the dispersion relationship of the coating layer.

$$n(\lambda) = A_n + 10^6 B_n / \lambda^2 + 10^{12} C_n / \lambda^4, \text{ where } \lambda \text{ (Wavelength) in nm} \tag{1}$$

$$k(\lambda) = A_k + 10^6 B_k / \lambda^2 + 10^{12} C_k / \lambda^4, \text{ where } \lambda \text{ (Wavelength) in nm} \tag{2}$$

The optical parameters of the TiO$_2$ layer were then determined from the measured transmittance and reflectance spectra for each coating by fitting simultaneously the results obtained from calculations and measurements over the 400~1000 nm region. The detailed fitting process can be founded in our previous work [30,31]. To judge the quality of the fitting, the root mean squared error (*RMSE*) was defined by:

$$RMSE = \sqrt{\sum_{j=1}^{n} [(Y_{\exp_j} - Y_{calc_j})^2 \times weight_j^2] \Big/ \sum_{j=1}^{n} weight_j^2}, \tag{3}$$

where *n* is the number of selected experimental data, Y_{exp} is the value of the experimental data, Y_{calc} is the calculated value and $weight_j$ is the weight of each experimental point. The lower the RMSE value, the better is the agreement between fit and experimental data. The calculated optical parameters of all the coatings are listed in Table 1. All the *RMSE* values are less than 1, which ensure the reliability of the determined optical constants.

Table 1. Caculated optical parameters of TiO$_2$ coatings.

Sample	A_n	B_n (nm)	C_n (nm)	A_k	B_k (nm)	C_k (nm)	Thickness d (nm)	*RMSE*
400 ℃	1.892	0.036	5.701×10^{-4}	3.508×10^{-3}	1.538×10^{-15}	2.567×10^{-10}	96.46	0.4452
500 ℃	1.958	0.040	1.704×10^{-3}	5.757×10^{-3}	2.629×10^{-13}	7.540×10^{-13}	89.94	0.6306
600 ℃	1.996	0.035	3.921×10^{-15}	7.965×10^{-3}	2.280×10^{-9}	1.259×10^{-9}	86.87	0.5689
700 ℃	2.127	0.051	1.255×10^{-3}	8.741×10^{-3}	2.054×10^{-12}	4.287×10^{-9}	70.70	0.4936
800 ℃	2.401	0.023	0.010	2.987×10^{-3}	4.708×10^{-3}	4.310×10^{-4}	61.81	0.8760
900 ℃	2.385	0.063	4.707×10^{-3}	0.011	5.985×10^{-11}	1.102×10^{-3}	61.02	0.3872

The determined refractive indices, as a function of wavelength for crystallized TiO$_2$ coatings annealed at different temperatures, are shown in Figure 4. Decreasing refractive index with wavelength indicates normal dispersion behavior. The data show that the refractive index increases with annealing temperature, from 1.98 to 2.57 at He-Ne laser wavelength of 633 nm. The highest refractive index of anatase TiO$_2$ coating reaches to 2.26, which was close to the bulk anatase TiO$_2$. At 700 ℃ annealed coating, the rapid increase of refractive index might due to the thermal induced growth of the grains which increased the packing density. Further increasing annealing temperatures promotes the transition of crystalline phase from anatase to rutile and the densification of the coating structures [32]. Therefore, the refractive index has another rapid increase at 800 ℃ annealed coating. As can be known from AFM analysis, the crystalline transformation not only increases the density of the coatings but also leaves pinholes, which will decrease the packing density of the coating. Thus, the refractive index of rutile TiO$_2$ coating (900 ℃ annealed) only has a slight increase compared with the mixed phase TiO$_2$ coating (800 ℃ annealed).

Figure 4. Refractive index dispersion of TiO$_2$ coatings annealed at different temperatures.
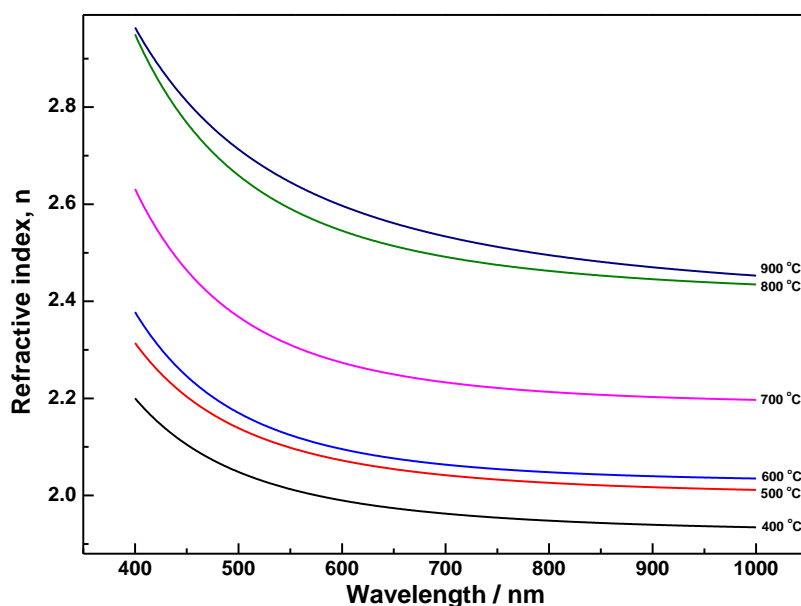
Also, it is noticeable from Figure 3 that all the coatings are transparent in the visible light region and their spectra exhibit a sharp decrease in the UV region (300~350 nm) because of the fundamental light absorption. From the measured transmittance *T*, given in Figure 3, we deduce the absorption coefficient *α* using the following relation [33]:

$$\alpha \approx \frac{1}{d} \ln \frac{1}{T} \tag{4}$$

where *d* is the thickness of the coating (Table 1) and *T* is its transmittance.

It is known that TiO$_2$ has direct and indirect band gaps [34]. To determine values of these forbidden energies, we use the expression in Equation (5). The relationship between the absorption coefficient *α* and the incident photon energy is given by the relation as follows [35]:

$$\alpha h v = A (h v - E_g)^m \tag{5}$$

where *A* is a constant depending on the transition probability and *m* is equal to 1/2 for a direct gap and 2 for an indirect gap. The usual method to calculate the band gap energies is to plot $(\alpha h v)^{1/m}$ as a function of the incident radiation energy (*hv*) [36]. The band gap values are then determined by extrapolating values of the absorption coefficient *α* to zero. Figure 5 is a typical plot of $(\alpha h v)^{1/m}$ *vs.* incident energy (*hv*). As represented in the figure, we found 3.86 and 3.22 eV for the direct and indirect band gap energies, respectively.

Figure 5. Plot of $(\alpha h v)^{1/m}$ *vs.* (*hv*) for the estimation of the band gap energy value (400 ℃ annealed TiO$_2$ coating): (**a**) indirect gap and (**b**) direct gap.
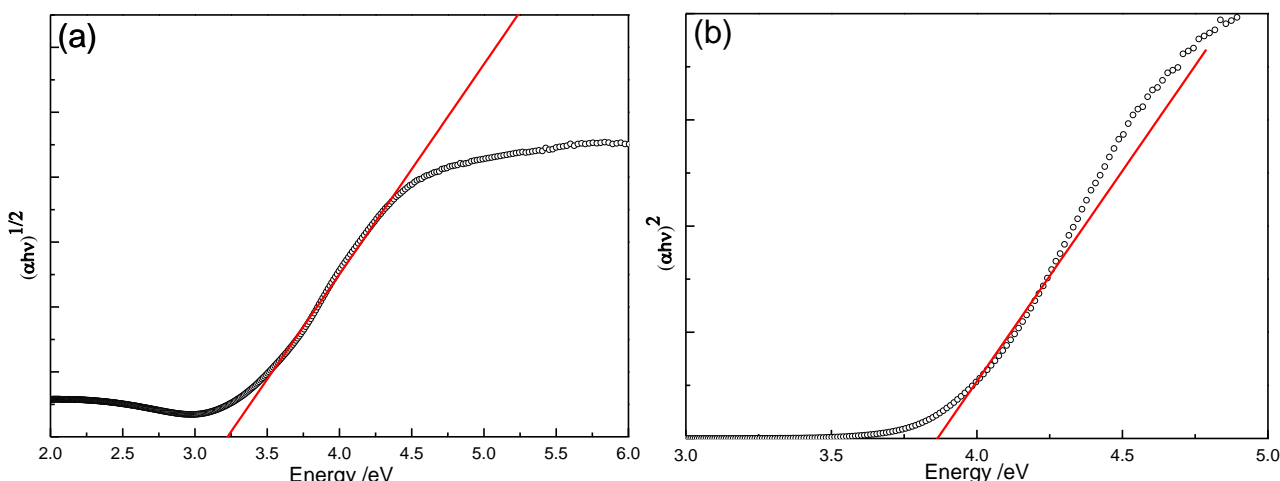
The same analysis procedure was repeated to obtain the band gaps for all the TiO$_2$ coatings annealed at different temperatures (as listed in Table 2). As can be seen, the direct band gap decreased from 3.86 to 3.65 eV with increasing of annealing temperature from 400 to 900 ℃, while the indirect band gap decreased from 3.22 to 2.93 eV. It is connected with the size of the grain. An increase of the grain size weakens quantum size effects, thereby causing the decrease of the band gap and red shift of the absorption edge.

Table 2. Band gap of TiO$_2$ coatings annealed at different temperatures.

Sample/℃	400	500	600	700	800	900
$E_{g\text{-}indirect}$/eV	3.22	3.17	3.15	3.09	2.97	2.93
$E_{g\text{-}direct}$/eV	3.86	3.82	3.79	3.77	3.67	3.65

3.3. Surface Morphology

The AFM imaging was performed to study the surface morphology changes induced by thermal annealing. Figure 6 shows the surface morphology of the coatings annealed at 300, 500, 700, and 900 ℃, respectively. Three hundred-degree Celsius annealed coating exhibits a smooth surface and very fine particles, indicating the amorphous structure of the coating. The root mean square roughness (R_q) of the surface is less than 1 nm and increases with the increasing treatment temperature, which indicates the grains of regular shapes develop on the surface.

Figure 6. 2D AFM images of TiO$_2$ coatings annealed at (**a**) 300 ℃; (**b**) 500 ℃; (**c**) 700 ℃; (**d**) 900 ℃.

(**a**) R_q = **0.214** nm   (**b**) R_q = **0.464** nm

(**c**) R_q = **1.356** nm   (**d**) R_q = **3.509** nm
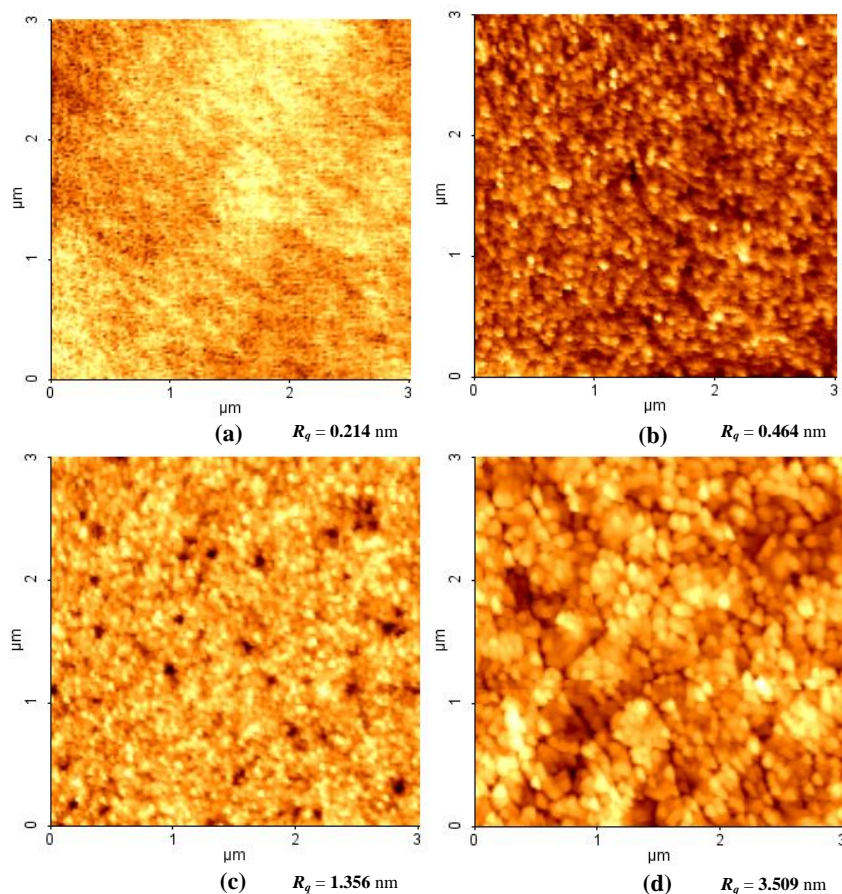
As can be seen from the Figure 6b (coating treated at 500 ℃), there is a preferred orientation of the regularly-shaped grains, which suggests the growth of the nano-crystalline TiO$_2$ grains. At temperatures of 700 ℃, the grains get larger and combine to make denser coatings, but the basic structure remains un-changed. After annealing up to 900 ℃, a significant increase of the grain size is observed and R_q increases to 3.509 nm. It is because the transformation of anatase into rutile went through the coalescence of smallest particles and formation of bigger particles [37], which then increase its grain size. The AFM results are in good agreement with Raman analysis, which shows structure changes during thermal annealing. Coating densification takes place with coating crystallization, as also revealed by AFM.

3.4. Stability of TiO₂ Sol

The sol stability plays an important role in obtaining the uniform TiO$_2$ coatings with a high optical quality, especially for industrial application. During the storage, the particles and clusters keep growing and the network keeps extending until the sol finally turns to a gel, which will affect the properties of the final products. Particle size distribution curve of as-synthesized sol, presented in Figure 7, shows a narrow distribution of titania particles with an average size of 7.4 nm. The measurement was repeated every 30 days to evaluate the stability in the long term storage at the room temperature. As the figure showed, the average size of the TiO$_2$ particles after 30 and 60 days are 8 and 10.6 nm, respectively. After being stored for 90 days, they increased to 14 nm, which is still in a sufficient condition for coating. This kind of gradual evolution can be attributed partly to the esterification reaction, which allows slow continuing further hydrolysis to occur and helps combine the particles with time [38,39]. This indicates that the reaction during the sol-gel process was controlled with a relatively optimized condition and can be used for coating in a relatively long time.

Figure 7. Particle size distribution of TiO$_2$ sol.
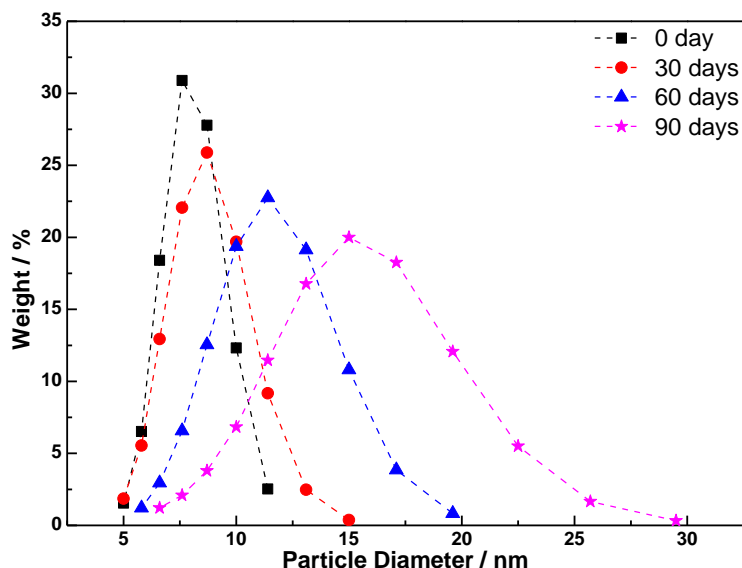
4. Conclusions

TiO$_2$ coatings have been deposited by the sol-gel method and the coatings were annealed at temperatures from 400 to 900 ℃ to realize crystallization. The Raman analysis show that the 400 ℃ annealed TiO$_2$ coatings are crystallized to the anatase phase and convert to the rutile phase after being annealed at 900 ℃. The obtained highest refractive index of anatase TiO$_2$ coating was 2.26. This value increased to 2.57 after further annealing, which can be explained by the development of the crystalline structure, the difference of surface morphology and the increase of the density of the coatings as indicated by AFM and Raman results.

Acknowledgments

Conflict of Interest

The authors declare no conflict of interest.

References

1. Bi, Z.-F.; Wang, L.; Liu, X.-H.; Zhang, S.-M.; Dong, M.-M.; Zhao, Q.-Z.; Wu, X.-L.; Wang, K.-M. Optical waveguides in TiO_2 formed by He ion implantation. *Opt. Express* **2012**, *20*, 6712–6719.

2. Szeghalmi, A.; Helgert, M.; Brunner, R.; Heyroth, F.; Gösele, U.; Knez, M. Atomic layer deposition of Al_2O_3 and TiO_2 multilayers for applications as bandpass filters and antireflection coatings. *Appl. Opt.* **2009**, *48*, 1727–1732.

3. Wang, X.; Shen, J. Sol-gel derived durable antireflective coating for solar glass. *J. Sol-Gel Sci. Technol.* **2010**, *53*, 322–327.

4. Peng, B.; Jungmann, G.; Jäger, C.; Haarer, D.; Schmidt, H.-W.; Thelakkat, M. Systematic investigation of the role of compact TiO_2 layer in solid state dye-sensitized TiO_2 solar cells. Coordin. *Chem. Rev.* **2004**, *248*, 1479–1489.

5. Sauvage, F.; di Fonzo, F.; Li Bassi, A.; Casari, C.S.; Russo, V.; Divitini, G.; Ducati, C.; Bottani, C.E.; Comte, P.; Graetzel, M. Hierarchical TiO_2 photoanode for dye-sensitized solar cells. *Nano Lett.* **2010**, *10*, 2562–2567.

6. Hamadanian, M.; Sayahi, H.; Zolfaghari, A. Modified multistep electrophoretic deposition of TiO_2 nanoparticles to prepare high quality thin films for dye-sensitized solar cell. *J. Mater. Sci.* **2012**, *47*, 5845–5851.

7. Yamada, Y.; Uyama, H.; Watanabe, S.; Nozoye, H. Deposition at low substrate temperatures of high-quality TiO_2 films by radical beam-assisted evaporation. *Appl. Opt.* **1999**, *38*, 6638–6641.

8. Eiamchai, P.; Chindaudom, P.; Pokaipisit, A.; Limsuwan, P. A spectroscopic ellipsometry study of TiO_2 thin films prepared by ion-assisted electron-beam evaporation. *Curr. Appl. Phys.* **2009**, *9*, 707–712.

9. Albertinetti, N.; Minden, H.T. Granularity in ion-beam-sputtered TiO_2 films. *Appl. Opt.* **1996**, *35*, 5620–5625.

10. Chao, S.; Wang, W.-H.; Hsu, M.-Y.; Wang, L.-C. Characteristics of ion-beam-sputtered high-refractive-index TiO_2-SiO_2 mixed films. *J. Opt. Soc. Am. A* **1999**, *16*, 1477–1483.

11. Walczak, M.; Oujja, M.; Marco, J.; Sanz, M.; Castillejo, M. Pulsed laser deposition of TiO$_2$: Diagnostic of the plume and characterization of nanostructured deposits. *Appl. Phys. A Mater.* **2008**, *93*, 735–740.

12. Gámez, F.; Plaza-Reyes, A.; Hurtado, P.; Guillén, E.; Anta, J.A.; Martínez-Haya, B.; Pérez, S.; Sanz, M.; Castillejo, M.; Izquierdo, J.G.; *et al*. Nanoparticle TiO$_2$ films prepared by pulsed laser deposition: Laser desorption and cationization of model adsorbates. *J. Phys. Chem. C* **2010**, *114*, 17409–17415.

13. Dzibrou, D.; Grishin, A.M.; Kawasaki, H.; Suda, Y.; Pankov, V.V. Tailoring optical properties of pulsed laser deposited TiO$_2$ films. *J. Phys. Conf. Ser.* **2008**, *100*, doi:10.1088/1742-6596/100/8/082035.

14. Ayouchi, R.; Casteleiro, C.; Schwarz, R.; Barrado, J.R.; Mart ń, F. Optical properties of TiO$_2$ thin films prepared by chemical spray pyrolysis from aqueous solutions. *Phys. Status Solidi C* **2010**, *7*, 933–936.

15. Battiston, G.A.; Gerbasi, R.; Gregori, A.; Porchia, M.; Cattarin, S.; Rizzi, G.A. PECVD of amorphous TiO$_2$ thin films: Effect of growth temperature and plasma gas composition. *Thin Solid Films* **2000**, *371*, 126–131.

16. McCurdy, P.R.; Sturgess, L.J.; Kohli, S.; Fisher, E.R. Investigation of the PECVD TiO$_2$–Si(100) interface. *Appl. Surf. Sci.* **2004**, *233*, 69–79.

17. Phadke, S.; Sorge, J.D.; Hachtmann, S.; Birnie, D.P., III. Broad band optical characterization of sol-gel TiO$_2$ thin film microstructure evolution with temperature. *Thin Solid Films* **2010**, *518*, 5467–5470.

18. Sankapal, B.R.; Lux-Steiner, M.C.; Ennaoui, A. Synthesis and characterization of anatase-TiO$_2$ thin films. *Appl. Surf. Sci.* **2005**, *239*, 165–170.

19. Chrysicopoulou, P.; Davazoglou, D.; Trapalis, C.; Kordas, G. Optical properties of very thin (<100 nm) sol-gel TiO$_2$ films. *Thin Solid Films* **1998**, *323*, 188–193.

20. Yusuf, M.M.; Imai, H.; Hirashima, H. Preparation of porous titania film by modified sol-gel method and its application to photocatalyst. *J. Sol-Gel Sci. Technol.* **2002**, *25*, 65–74.

21. Wen, T.; Gao, J.; Shen, J.; Zhou, Z. Preparation and characterization of TiO$_2$ thin films by the sol-gel process. *J. Mater. Sci.* **2001**, *36*, 5923–5926.

22. Wang, X.; Shen, J.; Pan, Q. Raman spectroscopy of sol-gel derived titanium oxide thin films. *J. Raman Spectrosc.* **2011**, *42*, 1578–1582.

23. Yao, J.K.; Huang, H.L.; Ma, J.Y.; Jin, Y.X.; Zhao, Y.A.; Shao, J.D.; He, H.B.; Yi, K.; Fan, Z.X.; Zhang, F.; Wu, Z.Y. High refractive index TiO$_2$ film deposited by electron beam evaporation. *Surf. Eng.* **2009**, *25*, 257–260.

24. Wang, H.; Hu, Y.; Zhang, L.; Li, C. Self-cleaning films with high transparency based on TiO$_2$ nanoparticles synthesized via flame combustion. *Ind. Eng. Chem. Res.* **2010**, *49*, 3654–3662.

25. Zhao, L.; Han, M.; Lian, J. Photocatalytic activity of TiO$_2$ films with mixed anatase and rutile structures prepared by pulsed laser deposition. *Thin Solid Films* **2008**, *516*, 3394–3398.

26. Wang, X.; Shen, J.; Wang, S.; Zhang, Z. Optical constants of sol-gel derived TiO$_2$ films characterized by spectroscopic ellipsometry. *Acta Phys. Sin.* **2009**, *58*, 8027–8032.

27. Ohsaka, T.; Izumi, F.; Fujiki, Y. Raman spectrum of anatase, TiO$_2$. *J. Raman Spectrosc.* **1978**, *7*, 321–324.

28. Zhang, W.F.; He, Y.L.; Zhang, M.S.; Yin, Z.; Chen, Q. Raman scattering study on anatase TiO_2 nanocrystals. *J. Phys. D Appl. Phys.* **2000**, *33*, 912–916.

29. Jenkins, F.A.; White, H.E. *Fundamentals of Optics*, 4th ed.; McGraw-Hill, Inc.: New York, NY, USA, 1981.

30. Wang, X.; Wu, G.; Zhou, B.; Shen, J. Improvement on laser-induced damage threshold of sol-gel ZrO_2 coatings by crystal structure tuning. *Opt. Express* **2012**, *20*, 24482–24487.

31. Wang, X.; Wu, G.; Zhou, B.; Shen, J. Effect of crystal structure on optical properties of sol-gel derived zirconia thin films. *J. Alloys Compd.* **2013**, *556*, 182–187.

32. Fabes, B.D.; Birnie, D.P., III; Zelinski, B.J.J. Porosity and composition effects in sol-gel derived interference filters. *Thin Solid Films* **1995**, *254*, 175–180.

33. Pankove, I. *Optical Processes in Semiconductors*; Prentice-Hall: Englewood Cliffs, NJ, USA, 1971.

34. Janitabar-Darzi, S.; Mahjoub, A.R.; Nilchi, A. Investigation of structural, optical and photocatalytic properties of mesoporous TiO_2 thin film synthesized by sol-gel templating technique. *Physica E* **2009**, *42*, 176–181.

35. Tauc, J.; Grigorovici, R.; Vancu, A. Optical properties and electronic structure of amorphous germanium. *Phys. Status Solidi* **1966**, *15*, 627–637.

36. Ghrairi, N.; Bouaicha, M. Structural, morphological, and optical properties of TiO_2 thin films synthesized by the electro phoretic deposition technique. *Nanoscale Res. Lett.* **2012**, *7*, doi:10.1186/1556-276X-7-357.

37. Richards, B.S. Novel Uses of Titanium Dioxide for Silicon Solar Cells. Ph.D. Thesis, University of New South Wales, Sydney, Australia, 2002.

38. Birnie, D.P., III; Bendzko, N.J. ^1H and ^{13}C NMR observation of the reaction of acetic acid with titanium isopropoxide. *Mater. Chem. Phys.* **1999**, *59*, 26–35.

39. Birnie, D.P., III. Esterification kinetics in titanium isopropoxide-acetic acid solutions. *J. Mater. Sci.* **2000**, *35*, 367–374.